

Article

Accurate Measurement of the Internal Temperature of 280 Ah Lithium-Ion Batteries by Means of Pre-Buried Thermocouples

Jiazheng Lu, Yang Lyu *, Baohui Chen and Chuaping Wu

State Key Laboratory of Disaster Prevention & Reduction for Power Grid, State Grid Hunan Electric Power Company Limited, Changsha 410000, China; lujz1969@163.com (J.L.); bymountains@gmail.com (B.C.); jandom@126.com (C.W.)

* Correspondence: lv_yang@buaa.edu.cn

Abstract: Batteries with an energy storage capacity of 280 Ah play a crucial role in promoting the development of smart grids. However, the inhomogeneity of their internal temperature cannot be accurately measured at different constant charge and discharge power, affecting the efficiency and safety of the battery. This work adopts finite element analysis to determine the typical internal temperature of a single-cell model, which can guide the measuring position of the battery. Before the manufacturing process, a slim pre-buried sensor is utilized to reduce the negative impacts of different constant charge and discharge powers. The maximum internal temperature of the battery is up to 77 °C at a constant charge and discharge power of 896 W. The temperature difference between the two poles and the battery surface is as high as 26.2 °C, which is beyond the safety temperature (55 °C). This phenomenon will result in the degradation of the positive electrode through dQ/dV curves. These measurements of battery internal temperature can improve battery heat control and facilitate the development of energy storage technology.

Keywords: internal temperature; degradation; lithium-ion battery; energy storage



Citation: Lu, J.; Lyu, Y.; Chen, B.; Wu, C. Accurate Measurement of the Internal Temperature of 280 Ah Lithium-Ion Batteries by Means of Pre-Buried Thermocouples. *Batteries* **2024**, *10*, 184. <https://doi.org/10.3390/batteries10060184>

Academic Editor: Federico Baronti

Received: 13 April 2024

Revised: 15 May 2024

Accepted: 20 May 2024

Published: 28 May 2024



Copyright: © 2024 by the authors. Licensee MDPI, Basel, Switzerland. This article is an open access article distributed under the terms and conditions of the Creative Commons Attribution (CC BY) license (<https://creativecommons.org/licenses/by/4.0/>).

1. Introduction

With the development of renewable energy, lithium-ion battery (LIB) energy storage systems have been developed on a large scale due to their high energy density, high efficiency, and long lifetime [1–6]. Historically, low-capacity power batteries with a capacity of less than 200 Ah have been the most commonly used in mobile vehicles. Due to their small size, there are no significant temperature differences between the interior and surface of these batteries [7]. Data from surface thermal sensors on LIBs can be used to perform appropriate thermal management, which allows the temperature of the battery to be controlled within a reasonable range and extended life to be achieved [8–10]. Temperature accumulation and conduction problems occur at the pack and system levels, rather than at the cell level. After the application of high-capacity lithium iron phosphate (LFP) batteries in energy storage, engineers noticed this issue and started to understand cell-level temperature distribution [11].

Recently, the 280 Ah wound lithium iron phosphate battery (71-battery), measuring 173 mm in length, 71 mm in thickness, and 204 mm in height, has achieved great success in the energy storage market. The large capacity of these batteries can simplify system complexity and reduce costs. However, the large thickness of the 71-battery, which has different thermal conductivity in different directions (thickness and planar), can lead to uneven temperature distribution when exposed to different constant charge and discharge power (P) [12,13]. Detecting rapid temperature fluctuations inside the battery with surface sensors is challenging [14]. Uneven temperature distribution may result in temperature-induced degradation, which will reduce battery performance, limit its calendar life, or even cause safety hazards [15].

There are ongoing efforts to improve the safety and longevity of lithium-ion batteries by measuring the difference between their external and internal temperatures [16]. Multiple approaches are employed in laboratories to accomplish this goal. These methods comprise the use of sensors, such as thermocouples [17,18], thermistors [19,20], resistance temperature detectors (RTDs) [21,22], or the direct measurement of internal temperature by means of optical fibers [23,24]. Some researchers employ commercial battery layouts with multiple temperature sensors for more accurate distribution. The installation of a sensor after the battery is assembled can have a negative impact on battery performance. It is worth mentioning that the temperature distribution of batteries can differ based on their size and capacity. The available data regarding internal battery temperature are primarily limited to small batteries and soft-pack batteries [25]. Insufficient analysis has been conducted on 280 Ah energy storage batteries. It is therefore crucial to develop and improve internal measurement plans accordingly.

An accurate lithium battery temperature distribution model can illustrate the heat production process in lithium-ion batteries and aid in the measurement of internal temperature distribution [26]. The lumped parameter model exhibits good performance in temperature prediction. The internal temperature of lithium batteries is based on a simplified electric–thermal coupling model. The thermal resistance heat transfer model describes the heat transfer process of batteries to estimate the internal temperature of batteries in real time [27]. The enhanced single-particle electrochemical model is used to construct an online estimation model of temperature and lithium concentration. Numerical simulation and experiments verified that this method has a good temperature estimation ability at different charge and discharge rates [28]. However, the lumped parameter model reduces the spatially distributed heat conduction process to several discrete points of heat flow, ignoring the spatial inhomogeneity of temperature distribution. The pseudo-two-dimensional (P2D) model adopts two spherical particles to model each electrode and assumes that the charge transfer reaction occurs uniformly within the electrode. This model is less accurate in estimating internal temperature [29]. Through the electrochemical–thermal model, variations in reversible and irreversible heat with the depth of discharge are studied. It is found that the lower the heat production of the fluid collector and the separator, the lower their influence on the temperature of the battery [30]. This work utilizes the electrochemical thermal model to guide internal temperature measurements.

Here, the finite element method is used to calculate the temperature distribution and extreme points of a single LFP battery. Then, micro-thermocouple sensors are pre-embedded in the battery manufacturing process. After battery capacity division, the explosion-proof valve is opened to lead out the signal wire and then resealed to minimize its impact on the battery's electrical performance. The differences in internal and external temperature increase in 280 Ah wound lithium iron phosphate batteries under different P during the charging and discharging process are determined, and the influence of the battery's high internal temperature is analyzed.

2. Materials and Methods

2.1. Battery Preparation

A slurry containing lithium iron phosphate as the cathode active material (95 wt%), carbon black (Super P, 2.5 wt%), and PVDF binder (2.5 wt%, PVDF–HFP, JuHua, Quzhou, China) in N-methyl-2-pyrrolidone (NMP, BingZhouYuNeng, Bingzhou, China) was homogenized for 5 h in a planetary stirrer. The liquid content of the lithium iron phosphate (Y9, HuNan YuNeng, Xiangtan, China) slurry was 60 wt%. The slurry was then cast on a carbon-coated Al foil (13 μm thickness), with a coating gap of 150 μm as specified on the film applicator. For LFP batteries, the fabricated electrode coatings had practical capacities of $4.9 \pm 0.1 \text{ mAh cm}^{-2}$ ($\sim 33 \text{ mg cm}^{-2}$). The capacities were calculated based on the 157 mAh g^{-1} practical capacities of LFP batteries. The coatings were dried in a vacuum oven at 130°C . Ambient humidity was $\text{RH} < 10\%$.

2.2. Cell Assembly and Electrochemical Characterization

LFP cells with an N/P ratio of ~1.1 were assembled in a square aluminum case format with four battery cores. All four battery cores were PE membranes (9 μm) with 6 μm ceramic coating. All electrodes were connected to aluminum current collectors (13 μm , thickness). Charging and discharging instruments (XingYun company, Guangzhou, China, NEEFLCT-10060-V002) were used to measure the electrochemical properties of the battery at a constant P, namely 224 W (0.5 P = 3.2 V \times 70 A), 448 W (1 P = 3.2 V \times 140 A), and 896 W (2 P = 3.2 V \times 280 A). The upper and lower limits of charge and discharge voltage were 3.65 and 2.5 V, respectively. After the charging process, there was a 30 min standing process before discharge. All galvanostatic cycling tests were carried out at room temperature (20–22 °C). A data recorder with T-type thermocouples was employed to reflect the temperature distributions of the battery. The influence of pre-buried thermocouples inside the battery was tested using an AC impedance meter.

3. Results and Discussion

3.1. The Location and Influence on the Battery with Thermocouples

In the battery manufacturing process, commercially available T-type thermocouples with a wire diameter of 0.05 mm were positioned externally on coil cores B and C (Figure 1a–c). This wire diameter of the T-type thermocouple can effectively prevent short circuits on the electrode plate. Additionally, the wire of the thermocouple with a 0.045 mm thickness was wrapped using adhesive tape to improve its insulation capacity. This can ensure that the signal is not distorted and that the battery does not short-circuit. As a result, the resistance between the positive and negative ear was about 4.12 M Ω under the 200 V alternating current voltage. Based on the temperature distribution results of the electrochemical thermocouple battery model, the central position of the winding core and the position that is 1.0 cm from the terminal ear could indicate the overall increase in the temperature of the battery. Therefore, thermocouples were located at each of the three positions (Figure 1b). The next step was to position the coil core of the thermocouple. The assembly, baking, liquid injection, formation, and volumetric processes were sequentially completed. The consistency of battery performance can be successfully ensured by following the same preparation process as the live battery. Before the experiment, the explosion-proof valve was opened to extract the sensing line of the thermocouple and then resealed. The narrow aperture guaranteed a secure seal and had minimal impact on battery performance. This allowed for the effective monitoring of the temperature distribution within the 280 Ah square lithium-ion energy storage battery as it was subjected to varying constant P. The T-type thermocouple was attached to the center of the battery surface to monitor the surface temperature of the battery.

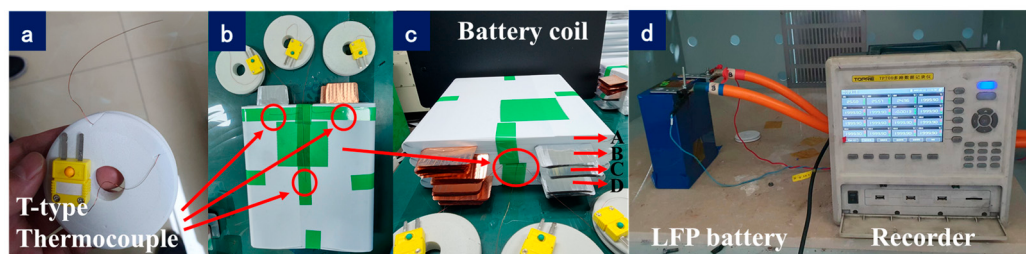


Figure 1. Installation and measurement process of the thermocouple: (a) T-type thermocouple; (b,c) the installation position of the thermocouple on the four-battery coil; (d) the layout of the experiment.

In order to evaluate the impact of installing thermocouples inside the battery on its performance, the internal resistance and electrical performance of two types of batteries using an AC internal resistance tester and a charge–discharge tester were measured. Figure 2a depicts the AC resistance of different batteries. It can be seen that the AC internal resistance of the blank battery was 0.150 m Ω , while that of the battery with a thermocouple installed

in situ was $0.153\text{ m}\Omega$. Additionally, the internal electronic resistance of the battery hardly changed. This is mainly due to the small diameter and good insulation of the thermocouple wire, which does not cause changes to the internal electronic circuit of the battery. The charging and discharging curves of different batteries before and after installing thermocouples with a constant P of 448 W are demonstrated. The charging capacity of the bare battery was 281.4 Ah . After installing the thermocouples, the charging of the battery was 280.6 Ah . The charging capacity of the battery hardly changed, compared to the coulombic efficiency (CE, 99.5%) of the reference battery, voltage efficiency (VE, 94.3%), and energy efficiency (EE, 93.8%). The CE, VE, and EE of the battery with a thermocouple installed were 99.5%, 93.1%, and 92.6%, respectively. This indicates that the battery has good sealing performance after installing the thermocouple, and gases such as oxygen, CO_2 , and water vapor in the air do not cause significant side reactions in the battery. The change in energy efficiency is mainly caused by the increase in the internal resistance of the battery itself.

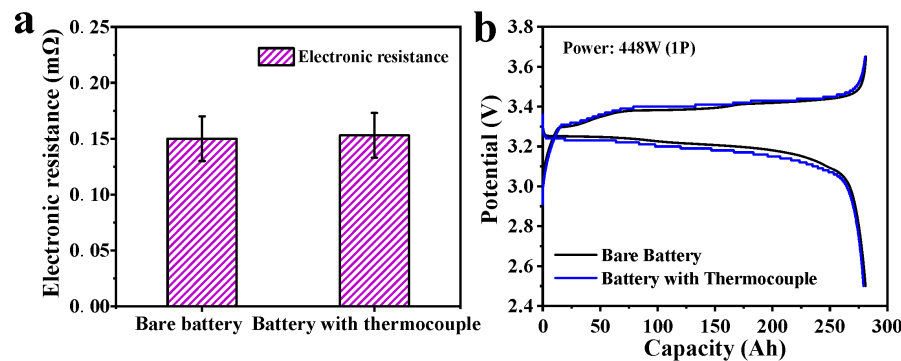


Figure 2. (a) The electronic resistance of the bare battery and the battery with the thermocouple; (b) the charge and discharge curves of the bare battery and battery with thermocouple at 448 W .

The electrochemical–thermal model is based on a number of theoretical principles, including porous electrode theory, Ohm’s law, mass transfer within the solid and electrolyte phase, concentrated solution theory, and the kinetics of intercalation and deintercalation. The reference exchange current density, particle radius, and thermal conductivity were the electrochemical parameters used in the model (Table S1). The temperature distribution and extreme points of the single battery model were calculated through the implementation of the finite element method (Figure 3). Figure S1 illustrates the experimental and numerical cell voltages for a charge and discharge rated at 0.5 P . The model, based on natural and simplified geometries, is capable of precisely predicting cell voltage, incorporating the electric drop generated by ohmic losses, charge-transfer overpotentials, and mass transfer limitations. It should be noted that there was a slight discrepancy between the cell voltage predicted by the model and that obtained from measurements due to the different geometries involved. The average relative errors between simulations and experiments for both geometries at 0.5 P were relatively low. Therefore, the electrical model was validated for both discharge and charge. When exposed to a constant of 0.5 P , the battery’s peak temperature was at the pole ear. In contrast, the base of the pole plate displayed the lowest temperature, with up to $1.6\text{ }^\circ\text{C}$ temperature gap (Figure 3a). Additionally, Figure 3b illustrates the contour line and corresponding aspects of the 71–battery. It should be noted that the heat source of the battery’s lug portion enhanced the role of the increased temperature for the region near two lugs of the pole piece, thus resulting in the warming of the entire battery. The battery’s temperature varied along its length, forming a gradient distribution with a more uniform and lower temperature at the bottom of the battery. This is due to the highest heating power at the pole ear, where all batteries intersected, which could reach a density of up to $2.539 \times 10^5\text{ W m}^{-3}$. Figure 3d illustrates the distribution of heating power for battery electrodes. The chart shows that the heating power increases as the electrode is closer to the ear and decreases as it moves toward the bottom. This can be explained by the clustering of current at the ear of the electrode. When the current density at the bottom of

the battery electrode is low, the current at the top of the battery electrode is concentrated, resulting in greater heating power.

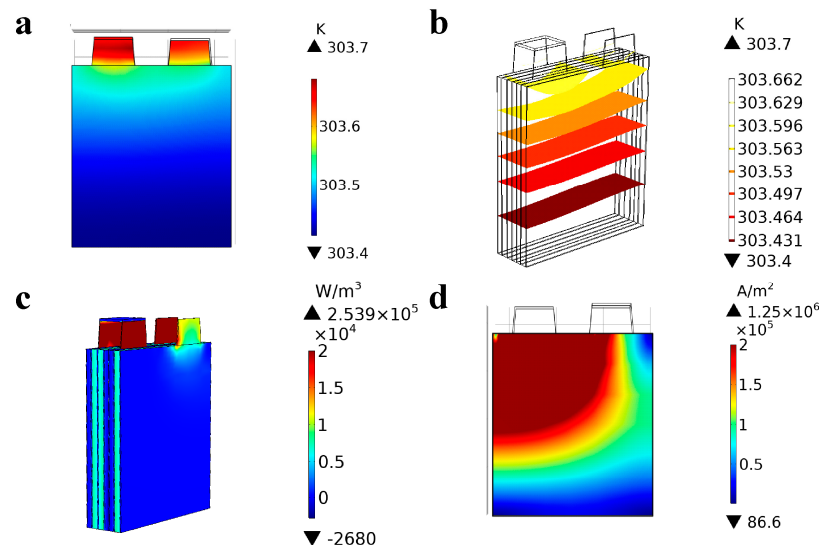


Figure 3. The results of the simulation of the battery at the end of one charging and discharging cycle: (a) the temperature distribution; (b) the isotherm line; (c) the heating rate; (d) the current density distribution of the single battery model.

3.2. The Battery's Internal Temperature and Its Influence

The charge–discharge curves and the increase in the temperature of the battery under different constant P are shown in Figure 4. The temperature of the battery under natural air convection exhibits fluctuations in the charge–discharge process, which is primarily due to the significant effect that the battery temperature has on the irreversible heat generated under low-power charge–discharge conditions. In thermal models, the generation of heat is commonly described as the sum of reversible and irreversible sources. Reversible heat is due to the change in open circuit voltage (OCV) with temperature, while irreversible heat is due to overpotential, including ohmic losses, charge transfer, overpotential and mass transfer limitations, and the formation of mixed heat. The heat from material phase transitions due to the diffusion of lithium ions in the solid phase is another source of irreversible heat [31]. Irreversible heat involves heat absorption and exothermic reaction with the state of charge (SOC) change. Additionally, the total heating power of the battery is constantly changing [23,24]. At this time, the maximum and minimum values of the internal temperature of the battery were $32.6\text{ }^{\circ}\text{C}$ and $26.7\text{ }^{\circ}\text{C}$, respectively (Figure 4a,b). The temperature difference between the three positions of this battery and the battery case surface was less than $2\text{ }^{\circ}\text{C}$. Upon the completion of the discharge process, the maximum temperature differential between the interior and exterior of the battery was $3.2\text{ }^{\circ}\text{C}$.

Under the constant power of 0.5 P , the temperature difference between the inside and outside of the battery was less than $5\text{ }^{\circ}\text{C}$, and the charge and discharge curves of the battery under different power conditions were normal (Figure 4a,b). When the constant charge and discharge power increased to 1P (448 W), the anode vicinity was at the maximum value of the present temperature at the end of discharge ($41.8\text{ }^{\circ}\text{C}$) (Figure 4c,d). It is worth noting that throughout the 1 P charge/discharge period, most of the temperature differences between the battery poles and the surface were greater than $5\text{ }^{\circ}\text{C}$, and the temperature at the cathode was higher than that near the anode. A significant difference in temperature will result in a notable polarization discrepancy within the battery, which will ultimately lead to the depletion of active lithium and a reduction in the battery's overall lifespan. When the charge and discharge power of the battery increased to 2 P , the battery had a maximum temperature of up to $77\text{ }^{\circ}\text{C}$ at the end of one charge and discharge process, at which point the cathode and anode temperatures were almost equal, and the temperatures at the surface

of the battery were both above 40 °C (Figure 4e,f). The temperature difference between the two poles and the battery surface was as high as 26.2 °C, while the temperature difference between the center and the surface region reached 12.1 °C. Such a high temperature inside the battery and the temperature difference between different parts of the battery cause serious side reactions and temperature difference polarization problems, reducing the cycle stability of the battery. Therefore, the internal temperature under different power conditions can be used to optimize the control strategies of the battery management system (BMS). When the internal temperature reaches a threshold value, the energy storage system should be run at a lower power. The surface temperature was 51.1 °C under 2 P. However, the temperature of the area near the electrode could reach 77.4 °C. The coulombic efficiency was about 99.36% at 2 P compared with the 99.94% efficiency of the battery at 1P (Figure S2). A low coulombic efficiency means a severe side reaction, which can result in the capacity degradation of the battery. There was a significant negative influence on the operation of the lithium-ion battery energy storage during 7000 cycles. As a result, the 280 Ah LFP battery is recommended for operation at the charge and discharge power of 486 W to reduce the influence of high temperature on its capacity degradation. Using the newest Chinese national standard GB/T 36276-2018, the cycle life of the energy storage battery was tested under the 1P condition [32]. The magnification tests of the energy storage battery indicate a lower capacity than that of the 2 P battery. Furthermore, the operating power of the high-capacity energy storage battery should be determined using the internal temperature in order to avoid severe capacity degradation.

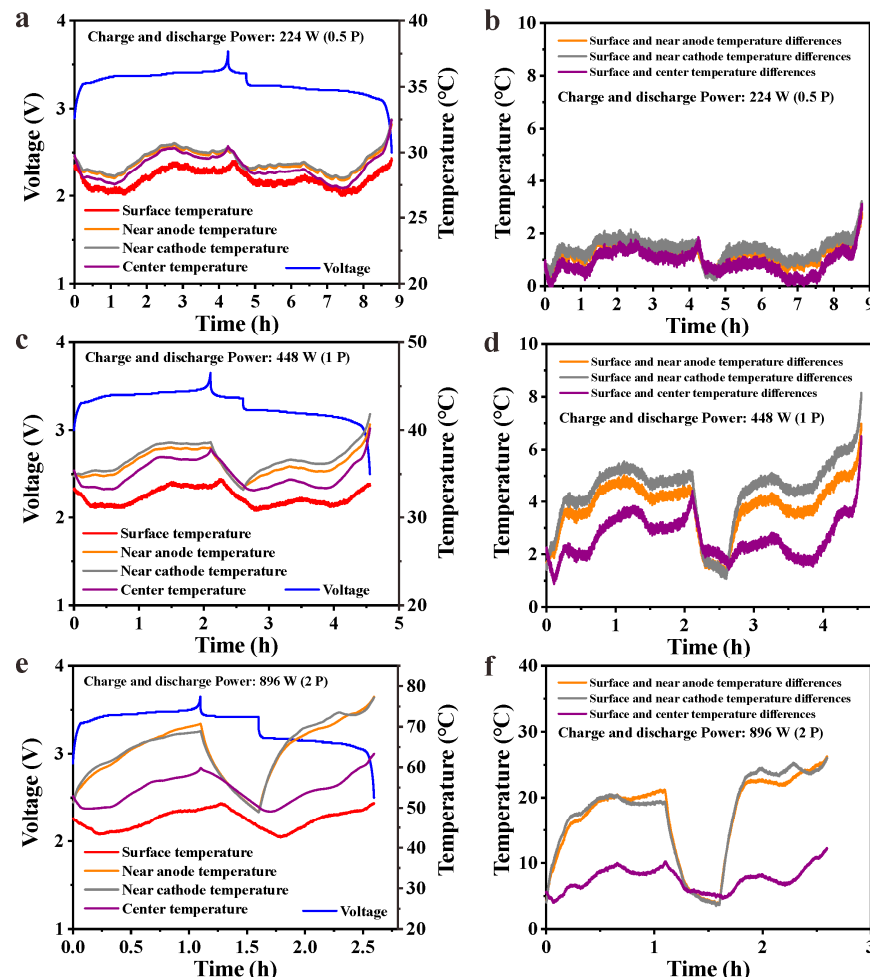


Figure 4. Temperature distribution curve and temperature differences of 280 Ah energy storage battery with thermocouple under different charging and discharging power: (a,b) 224 W; (c,d) 448 W; (e,f) 896 W.

The impact of an elevated internal temperature on battery performance was examined using the capacity curve. Battery A, which had heat dissipation, recorded surface and center internal temperatures of only 41.2 °C and 50.3 °C, while Battery B registered temperatures of 53.7 °C and 77.0 °C, respectively, without any heat dissipation. Batteries A and B exhibited similar characteristics during the initial third of their charge cycle, suggesting comparable amounts of residual lithium at the anode during the early stages of charging (Figure 5a). The battery displayed a coulombic efficiency nearing 100%. To assess the capacity loss across various internal temperatures, the differential capacity curve (dQ/dV) was employed and analyzed (Figure 5b). During the battery charge process, the curve exhibits three prominent peaks, which can be attributed to the presence of embedded lithium platforms in graphite. The peak area of dQ/dV can be calculated to obtain the lithium embedded capacity of each platform of graphite, and the active lithium loss and active site loss (or blocked) of the anode can be derived from the loss of capacity [25]. Compared to Battery A, Battery B exhibits an obvious decrease in the volume of Peak 1, Peak 2, and Peak 3. This phenomenon indicates that until reaching 77 °C, the internal temperature of Battery B results in an active graphite loss, which will reduce battery life.

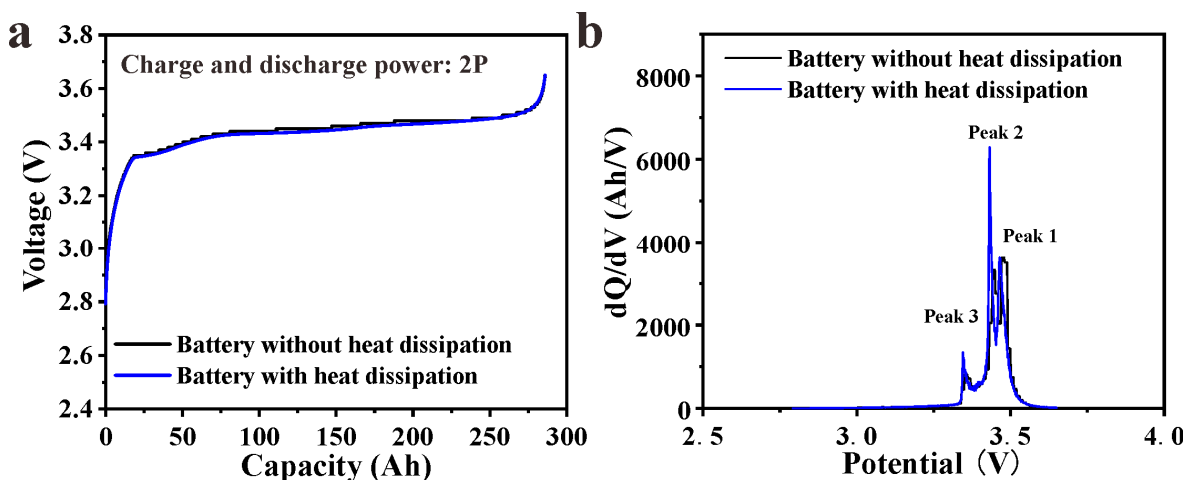


Figure 5. (a) The charge curve of the battery in different heat dissipation conditions; (b) the dQ/dV curve of the charge process.

The results of an overcharge test performed according to the Chinese national standard GB/T 36276-2018 “Lithium-ion battery for electrical energy storage” are shown in Figure 6. In 280 Ah batteries, the 100% state of charge is charging under 280 A. The cutoff voltage was set to 5.475 V. As the temperature of the pole ear was the highest among the batteries, the thermocouple was assembled near the pole ear on the surface of the battery. During the charging process, the temperature and voltage increased before reaching 83.9 °C. Once the surface temperature of the battery reached 83.9 °C, the temperature increase occurred very rapidly until the battery underwent thermal runaway (Figure 6). Under the 280 A charging process, there were about 26.2 °C temperature differences between the internal area and the surface area of the battery. The temperature of the internal area could reach about $83.9 + 26.2 = 110$ °C, which is over the melting point (108–126 °C) of the polyethylene membrane. Once the membrane began to melt, there was an internal shortage between the positive and negative electrodes, which led to the thermal runaway of the battery. The operating temperature control of the BMS should be set according to the highest temperature point of the battery under different charge and discharge processes to avoid thermal runaway and battery degradation.

Cyclic performance tests were carried out to verify the stability of this internal temperature distribution measurement method, and the results are shown in Figure 7. A successive charging and discharging process at 1 P (two cycles), 0.5 P (two cycles), and 2 P (three cycles) are exhibited in Figure 6. In the 1 P and 0.5 P power densities, the temperature was

stable in two cycles. In the 2 P power density, the temperature was stable in three cycles. Moreover, there were no obvious temperature changes in different cycles under the same constant charge and discharge power. The data collected from the sensor are representative and accurate.

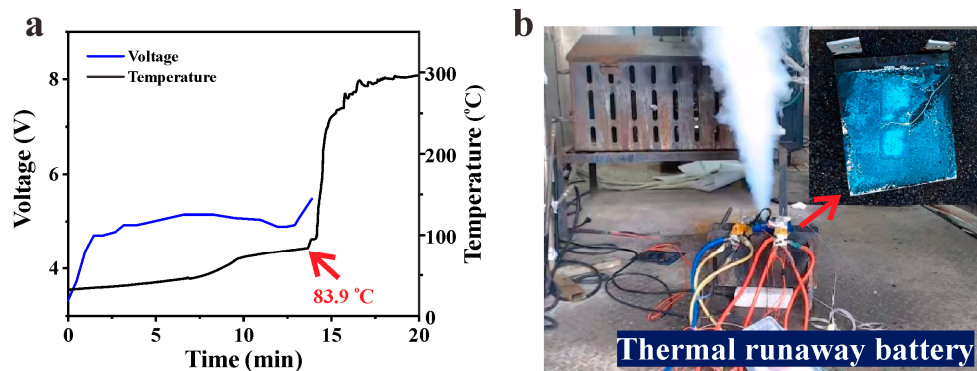


Figure 6. (a) The voltage and temperature of the battery in an overcharge test; (b) the image of the thermal runaway battery.

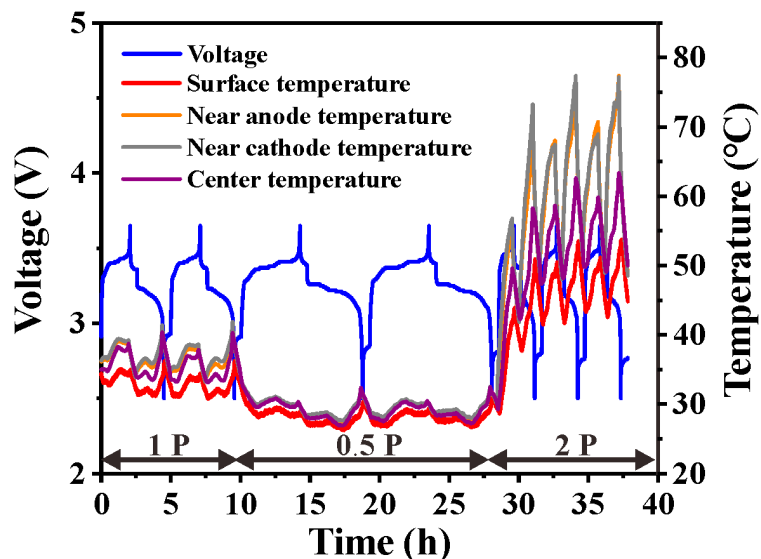


Figure 7. Cyclic performance tests.

4. Conclusions

In this work, the internal temperature distribution characteristics of the 280 Ah battery were determined. The battery pole lug and center areas were selected to pre-bury a slim 0.5 mm diameter thermocouple through finite element analysis. There was no negative effect on the thermocouples used in the battery based on the resistance test and electrochemical measurement results. At the end of the 0.5 P discharge process, the maximum temperature difference between the inside and outside of the battery was 3.2 °C. However, when the constant charge and discharge power increased to 2 P, the temperature difference between the two poles and the battery surface was as high as 26.2 °C. The temperature difference between the center and the surface also reached 12.1 °C. A high temperature inside the battery without a proper heat dissipation mode results in a huge temperature difference in the battery. The serious side reactions and polarization problems associated with temperature differences affect the cycle stability of the battery. Moreover, although the surface temperature was below the melting point of the membrane, the battery could undergo thermal runaway due to the high internal temperature. It is therefore essential to set the operating temperature control of the battery management system according to the internal temperature distribution.

Supplementary Materials: The following supporting information can be downloaded at: <https://www.mdpi.com/article/10.3390/batteries10060184/s1>, Figure S1. The charge and discharge curves of the simulated model and the real 280 Ah battery; Figure S2. The charge and discharge curves of the LFP battery under 1 P and 2 P; Table S1. The elements of the finite element method.

Author Contributions: Conceptualization, methodology, investigation, resources data and writing—review and editing Y.L.; formal analysis, B.C.; supervision, C.W.; funding acquisition, J.L. All authors have read and agreed to the published version of the manuscript.

Funding: This research was supported by the Science and Technology Project of State Grid Corporation of China under Grant No. 5108-202218280A-2-252-XG.

Data Availability Statement: The original contributions presented in the study are included in the article; further inquiries can be directed to the corresponding author.

Conflicts of Interest: Authors are employed by the State Grid Hunan Electric Power Company Limited.

References

- Lin, J.; Zhang, X.; Fan, E.; Chen, R.; Wu, F.; Li, L. Carbon neutrality strategies for sustainable batteries: From structure, recycling, and properties to applications. *Energy Environ. Sci.* **2023**, *16*, 745–791. [[CrossRef](#)]
- Fan, E.; Li, L.; Wang, Z.; Lin, J.; Huang, Y.; Yao, Y.; Chen, R.; Wu, F. Sustainable Recycling Technology for Li-Ion Batteries and Beyond: Challenges and Future Prospects. *Chem. Rev.* **2020**, *120*, 7020–7063. [[CrossRef](#)] [[PubMed](#)]
- Brand, M.J.; Hofmann, M.H.; Schuster, S.S.; Keil, P.; Jossen, A. The Influence of Current Ripples on the Lifetime of Lithium-Ion Batteries. *IEEE Trans. Veh. Technol.* **2018**, *67*, 10438–10445. [[CrossRef](#)]
- Alimardani, M.; Narimani, M. A New Energy Storage System Configuration to Extend Li-Ion Battery Lifetime for a Household. *IEEE Can. J. Electr. Comput. Eng.* **2021**, *44*, 171–178. [[CrossRef](#)]
- Qin, Z.; Zhang, T.; Gao, X.; Luo, W.; Han, J.; Lu, B.; Zhou, J.; Chen, G. Self-Reconstruction of Highly Degraded $\text{LiNi}_{0.8}\text{Co}_{0.1}\text{Mn}_{0.1}\text{O}_2$ toward Stable Single-Crystalline Cathode. *Adv. Mater.* **2024**, *36*, 2307091. [[CrossRef](#)]
- Qin, Z.; Zhang, Y.; Luo, W.; Zhang, T.; Wang, T.; Ni, L.; Wang, H.; Zhang, N.; Liu, X.; Zhou, J.; et al. A Universal Molten Salt Method for Direct Upcycling of Spent Ni-rich Cathode towards Single-crystalline Li-rich Cathode. *Angew. Chem. Int. Ed. Engl.* **2023**, *62*, e202218672. [[CrossRef](#)] [[PubMed](#)]
- Wang, J.; Sun, X. Olivine LiFePO_4 : The remaining challenges for future energy storage. *Energy Environ. Sci.* **2015**, *8*, 1110–1138. [[CrossRef](#)]
- Naik, I.; Nandgaonkar, M. Experimental Investigation of the Collective Impact of Electric Current and Ambient Temperature on the Thermal and Electrical Parameters of Lithium Iron Phosphate Cells. *Energy Technol.* **2021**, *9*, 2100593. [[CrossRef](#)]
- Wang, S.; Li, K.; Tian, Y.; Wang, J.; Wu, Y.; Ji, S. Improved thermal performance of a large laminated lithium-ion power battery by reciprocating air flow. *Appl. Therm. Eng.* **2019**, *152*, 445–454. [[CrossRef](#)]
- Basic, H.; Pandzic, H.; Miletic, M.; Pavic, I. Experimental Testing and Evaluation of Lithium-Ion Battery Cells for a Special-Purpose Electric Vacuum Sweeper Vehicle. *IEEE Access* **2020**, *8*, 216308–216319. [[CrossRef](#)]
- Wickramanayake, T.; Javadipour, M.; Mehran, K. A Novel Solver for an Electrochemical–Thermal Ageing Model of a Lithium-Ion Battery. *Batteries* **2024**, *10*, 126. [[CrossRef](#)]
- Tardy, E.; Thivel, P.-X.; Druart, F.; Kuntz, P.; Devaux, D.; Bultel, Y. Internal temperature distribution in lithium-ion battery cell and module based on a 3D electrothermal model: An investigation of real geometry, entropy change and thermal process. *J. Energy Storage* **2023**, *64*, 7090. [[CrossRef](#)]
- Peng, Y.; Zeng, L.; Dai, S.; Liu, F.; Rao, X.; Zhang, Y. LiFePO_4/C twin microspheres as cathode materials with enhanced electrochemical performance. *RSC Adv.* **2023**, *13*, 6983–6992. [[CrossRef](#)] [[PubMed](#)]
- Wang, S.; Ji, S.; Zhu, Y. A comparative study of cooling schemes for laminated lithium-ion batteries. *Appl. Therm. Eng.* **2021**, *182*, 116040. [[CrossRef](#)]
- Gulsoy, B.; Vincent, T.A.; Sansom, J.E.H.; Marco, J. In-situ temperature monitoring of a lithium-ion battery using an embedded thermocouple for smart battery applications. *J. Energy Storage* **2022**, *54*, 105260. [[CrossRef](#)]
- Raijmakers, L.H.J.; Danilov, D.L.; Eichel, R.A.; Notten, P.H.L. A review on various temperature-indication methods for Li-ion batteries. *Appl. Energer* **2019**, *240*, 918–945. [[CrossRef](#)]
- Heubner, C.; Schneider, M.; Lämmel, C.; Langlotz, U.; Michaelis, A. In-operando temperature measurement across the interfaces of a lithium-ion battery cell. *Electrochim. Acta* **2013**, *113*, 730–734. [[CrossRef](#)]
- Mutyala, M.S.K.; Zhao, J.; Li, J.; Pan, H.; Yuan, C.; Li, X. In-situ temperature measurement in lithium ion battery by transferable flexible thin film thermocouples. *J. Power Sources* **2014**, *260*, 43–49. [[CrossRef](#)]
- Vincent, T.A.; Gulsoy, B.; Sansom, J.E.H.; Marco, J. Development of an in-vehicle power line communication network with in-situ instrumented smart cells. *Transp. Eng.* **2021**, *6*, 100098. [[CrossRef](#)]
- Fleming, J.; Amietszajew, T.; Charmet, J.; Roberts, A.J.; Greenwood, D.; Bhagat, R. The design and impact of in-situ and operando thermal sensing for smart energy storage. *J. Energy Storage* **2019**, *22*, 36–43. [[CrossRef](#)]

21. Lee, C.-Y.; Lee, S.-J.; Tang, M.-S.; Chen, P.-C. In Situ Monitoring of Temperature inside Lithium-Ion Batteries by Flexible Micro Temperature Sensors. *Sensors* **2011**, *11*, 9942–9950. [[CrossRef](#)]
22. Zhu, S.; Han, J.; An, H.-Y.; Pan, T.-S.; Wei, Y.-M.; Song, W.-L.; Chen, H.-S.; Fang, D. A novel embedded method for in-situ measuring internal multi-point temperatures of lithium ion batteries. *J. Power Sources* **2020**, *456*, 227981. [[CrossRef](#)]
23. Momma, T.; Matsunaga, M.; Mukoyama, D.; Osaka, T. Ac impedance analysis of lithium ion battery under temperature control. *J. Power Sources* **2012**, *216*, 304–307. [[CrossRef](#)]
24. Novais, S.; Nascimento, M.; Grande, L.; Domingues, M.; Antunes, P.; Alberto, N.; Leitão, C.; Oliveira, R.; Koch, S.; Kim, G.; et al. Internal and External Temperature Monitoring of a Li-Ion Battery with Fiber Bragg Grating Sensors. *Sensors* **2016**, *16*, 1394. [[CrossRef](#)] [[PubMed](#)]
25. Chalise, D.; Shah, K.; Halama, T.; Komsiyska, L.; Jain, A. An experimentally validated method for temperature prediction during cyclic operation of a Li-ion cell. *Int. J. Heat Mass Transf.* **2017**, *112*, 89–96. [[CrossRef](#)]
26. Chen, L.G.; Hu, M.H.; Cao, K.B.; Li, S.X.; Su, Z.; Jin, G.Q.; Fu, C.Y. Core temperature estimation based on electro-thermal model of lithium-ion batteries. *Int. J. Energ Res.* **2020**, *44*, 5320–5333. [[CrossRef](#)]
27. Zhang, C.; Li, K.; Deng, J. Real-time estimation of battery internal temperature based on a simplified thermoelectric model. *J. Power Sources* **2016**, *302*, 146–154. [[CrossRef](#)]
28. Wang, P.; Yang, L.; Wang, H.; Tartakovsky, D.M.; Onori, S. Temperature estimation from current and voltage measurements in lithium-ion battery systems. *J. Energy Storage* **2021**, *34*, 102133. [[CrossRef](#)]
29. Zhang, D.; Popov, B.N.; White, R.E. Modeling Lithium Intercalation of a Single Spinel Particle under Potentiodynamic Control. *J. Electrochem. Soc.* **2000**, *147*, 831. [[CrossRef](#)]
30. Lai, Y.; Du, S.; Ai, L.; Ai, L.; Cheng, Y.; Tang, Y.; Jia, M. Insight into heat generation of lithium ion batteries based on the electrochemical-thermal model at high discharge rates. *Int. J. Hydrogen Energy* **2015**, *40*, 13039–13049. [[CrossRef](#)]
31. Bai, Y.; Li, L.; Li, Y.; Chen, G.; Zhao, H.; Wang, Z.; Wu, C.; Ma, H.; Wang, X.; Cui, H.; et al. Reversible and irreversible heat generation of NCA/Si-C pouch cell during electrochemical energy-storage process. *J. Energy Chem.* **2019**, *29*, 95–102. [[CrossRef](#)]
32. GB/T 36276-2018; Lithium Ion Battery for Electrical Energy Storage. Standardization Administration of China: Beijing, China, 2018.

Disclaimer/Publisher’s Note: The statements, opinions and data contained in all publications are solely those of the individual author(s) and contributor(s) and not of MDPI and/or the editor(s). MDPI and/or the editor(s) disclaim responsibility for any injury to people or property resulting from any ideas, methods, instructions or products referred to in the content.